Eur Radiol (2010) 20: 1311–1320
DOI 10.1007/s00330-009-1672-3

Mayil S. Krishnam
Anderanik Tomasian
Sachin Malik
Vibhas Desphande
Gerhard Laub
Stefan G. Ruehm

Image quality and diagnostic accuracy of unenhanced SSFP MR angiography compared with conventional contrast-enhanced MR angiography for the assessment of thoracic aortic diseases

Received: 4 June 2009
Revised: 26 August 2009
Accepted: 30 September 2009

M. S. Krishnam (✉)
Cardiovascular and Thoracic Imaging,
UCI Medical Center,
University of California,
333 City Boulevard West, Suite 1405,
Irvine, CA, 92868, USA
e-mail: mayilkrishnam@gmail.com
Tel.: +1-714-4562216
Fax: +1-714-4567864

A. Tomasian · S. Malik · S. G. Ruehm
Department of Radiological Sciences,
Ronald Reagan Medical Center,
University of California at Los Angeles,
Los Angeles, CA, USA

V. Desphande · G. Laub
Siemens Medical Solutions,
Los Angeles, CA, USA

Abstract *Objectives:* The purpose of this study was to determine the image quality and diagnostic accuracy of three-dimensional (3D) unenhanced steady state free precession (SSFP) magnetic resonance angiography (MRA) for the evaluation of thoracic aortic diseases. *Methods:* Fifty consecutive patients with known or suspected thoracic aortic disease underwent free-breathing ECG-gated unenhanced SSFP MRA with non-selective radiofrequency excitation and contrast-enhanced (CE) MRA of the thorax at 1.5T. Two readers independently evaluated the two datasets for image quality in the aortic root, ascending aorta, aortic arch, descending aorta, and origins of supra-aortic arteries, and for abnormal findings. Signal-to-noise ratio (SNR) and contrast-to-noise ratio (CNR) were determined for both datasets. Sensitivity, specificity, and diagnostic accuracy of unenhanced SSFP MRA for the diagnosis of aortic abnormalities were determined. *Results:* Abnormal aortic findings, including aneurysm (n=47), coarctation (n=14), dissection (n=12), aortic graft (n=6), intramural hematoma (n=11), mural thrombus in the aortic arch (n=1), and penetrating aortic ulcer (n=9), were confidently detected on both datasets. Sensitivity, specificity, and diagnostic accuracy of SSFP MRA for the detection of aortic disease were 100% with CE-MRA serving as a reference standard. Image quality of the aortic root was significantly higher on SSFP MRA (P<0.001) with no significant difference for other aortic segments (P>0.05). SNR and CNR values were higher for all segments on SSFP MRA (P<0.01). *Conclusion:* Our results suggest that free-breathing navigator-gated 3D SSFP MRA with non-selective radiofrequency excitation is a promising technique that provides high image quality and diagnostic accuracy for the assessment of thoracic aortic disease without the need for intravenous contrast material.

Keywords SSFP MR angiography · Unenhanced MRA · Thoracic aorta · Contrast · Enhanced MRA · Steady state free precession

Introduction

High spatial resolution contrast-enhanced magnetic resonance angiography (CE-MRA) [1–4] and multi-slice computed tomography angiography (CTA) [5, 6] are established non-invasive imaging techniques in the evaluation of thoracic aortic diseases with high diagnostic accuracy. In most institutions these techniques have replaced the previous reference standard, digital subtraction angiography (DSA), for diagnostic imaging of the thoracic aorta. In an acute clinical setting many institutions utilize CTA as the primary imaging technique to assess thoracic aortic aneurysm, aneurysmal rupture, aortic dissection, vasculitis, extracardiac anatomy of the great vessels in congenital heart diseases, and other acute aortic syndromes such as intramural hematomas and penetrating ulcerative plaques [5, 6]. Disadvantages of using CTA and DSA include the use of potentially nephrotoxic contrast agents and exposure to large amounts of radiation, especially when repeated acquisitions are performed [6]. Consequently, CE-MRA has been increasingly favored by many clinicians and radiologists in the follow-up assessment of patients with aortic dissection, aneurysm, coarctation, or graft repair, especially given the absent exposure to ionizing radiation.

However, this technique requires cooperation of the patient for breath-holding and administration of gadolinium-based contrast materials which may be contraindicated or not feasible, as in pregnancy or poor intravenous (IV) access. Although extremely rare, recent reports linking high-dose gadolinium-based contrast agents and nephrogenic systemic fibrosis (NSF) in patients with markedly impaired renal function, have questioned the safety of some of these agents in susceptible patients [7–9]. As a result, there has been an increased focus on the use of unenhanced MRA strategies in the depiction of vascular structures.

Unenhanced MRA techniques such as two-dimensional (2D) and three-dimensional (3D) time-of-flight sequences are sensitive to flow-related artifacts and are time consuming to image the entire thoracic aorta [10]. Steady state free precession (SSFP) MR imaging sequence allows increased intravascular signal-to-noise ratio (SNR) for improved visualization of vascular structures [11]. Recently, free-breathing cardiac and respiratory gated 3D SSFP MRA using non-selective radiofrequency (RF) excitation has been shown to be a promising novel technique in the assessment of major thoracic vessels. The use of this technique overcomes documented pitfalls of 2D SSFP, such as artifacts due to sensitivity to magnetic B0 field inhomogeneity, as thin-slice 2D SSFP requires longer TR/TE than possible with equivalent voxel resolution with 3D SSFP, and reduces out-of-slice contributions due to the non-selective RF excitation approach [12, 13].

The purpose of this study was to determine the image quality and diagnostic accuracy of free-breathing navigator-gated unenhanced 3D SSFP MRA using non-selective radiofrequency excitation for the evaluation of thoracic aortic diseases using CE-MRA as the reference standard.

Materials and methods

Patients

Our study was Health Insurance Portability and Accountability Act (HIPAA) compliant and approved by the institutional review board. Written informed consent was obtained from all participants. Fifty consecutive patients (30 male; 20 female; mean age 48.1 ± 14.2 years; age range 28–77 years) were examined with MR imaging. Clinical indications for the imaging included follow-up for known aortic aneurysm (n=19), coarctation (n=9), and dissection (n=7), and evaluation for suspected coarctation (n=2), dissection (n=3), and aneurysm (n=10). Clinical diagnoses of patients with known or suspected aortic aneurysm included congenital heart disease (n=7), Marfan's syndrome (n=5), bicuspid aortic valve disease (n=2), and atherosclerotic aortic disease (n=15). All patients were in sinus rhythm during the imaging with a heart rate less than 85 beats per minute. Exclusion criteria included any contraindication to MR imaging such as an implanted cardiac pacemaker or claustrophobia.

Image acquisition

All examinations were performed using 32-channel 1.5-Tesla MR imaging (Magnetom Avanto, Siemens Medical Solutions, Malvern, Pa., USA) with a maximum gradient amplitude of 45 mT/m and maximum slew rate of 200 mT/m/ms along each physical axis.

Before the examination a 20-gauge IV catheter was placed in an antecubital vein for contrast agent injection. Patients were examined in the supine position and advanced head first toward the magnet bore. A six-element body matrix and a six-element spine matrix coil were used for signal reception. Multiplanar scout images were obtained with a SSFP sequence.

Unenhanced MRA

Using a 3D, segmented SSFP sequence with non-selective radiofrequency excitation, unenhanced MRA of the whole chest was performed. To minimize cardiac motion artifacts, ECG-triggering with data acquisition during diastole was applied. Patients were not required to hold their breath during the MR data acquisition for this sequence.

To cover the whole chest and upper abdomen a large field of view (FOV) was selected and data acquisition was performed in coronal orientation with right to left phase encoding direction. The slab thickness was chosen to cover the entire chest coronally to avoid wrap-around slices due to the non-slice-selective RF excitation. T2 preparation (TE: 40 ms) [14, 15] was applied before data acquisition in each heartbeat to increase the blood pool-myocardial contrast. To reduce breathing-motion artifacts, a respiratory navigator-gated technique with prospective slice-following was applied. The navigator signal was created with a spin-echo sequence and tilted excitation and refocusing planes. Two intersecting slices were placed on the dome of the diaphragm for detection of respiratory motion (Fig. 1). To track the diaphragm for a stable respiratory phase throughout MR data acquisition, a 4-mm narrow respiratory gating window was used. The data acquired in each cardiac segment were accepted if the end-expiratory data fell within the pre-determined narrow 4-mm respiratory gating window. The remainder of the data falling outside this gating window were automatically rejected. An adaptive navigator-gating algorithm [16] was also implemented to compensate for respiratory drift along the relatively long free-breathing data acquisition, and to search for the end expiratory position of the diaphragm. After the navigator pulses, a frequency-selective fat saturation pulse was applied to suppress the fat signal followed by a non-selective RF excitation during the SSFP preparation and data acquisition. At the end of data acquisition, a gradient spoiler was used to avoid spillover of the protons' transverse magnetization into the next R-R interval.

The imaging parameters implemented for SSFP MRA were: field-of-view (FOV) 400×400 mm^2, flip angle 90°, readout bandwidth 980 Hz/pixel, matrix size 256×256 leading to true in-plane resolution of 1.6×1.6 mm^2, TE 1.0 ms, TR 2.3 ms. A total of 44–64 slices were measured with a slice thickness of 3 mm interpolated to 88–128 slices of 1.5 mm. During each cardiac cycle, 51–77 lines were measured depending on the heart rate. A parallel imaging technique, generalized autocalibrating partially parallel acquisition (GRAPPA) [17], with an acceleration factor of two, was implemented to shorten the MR data acquisition. Data acquisition was performed in coronal orientation as described above, with a navigator acceptance rate of 30–60% resulting in an imaging time for this sequence of 5–10 min (mean ± standard deviation, 7±2 min).

Conventional high spatial resolution 3D MRA

A 2-ml timing bolus was injected to determine the contrast material arrival time in the ascending aorta. Breath-hold high spatial resolution non-cardiac gated 3D CE-MRA of the thorax was acquired in coronal orientation using a gradient recalled echo (GRE) sequence during injection of 0.2 mmol/kg of gadopentetate dimeglumine (Magnevist, Berlex Laboratories, Wayne, N.J., USA) at 1.5 ml/s, followed by 20 ml of saline at the same rate using an electronic power injector (Spectris Solaris, Medrad, Indianola, Pa., USA). Imaging parameters were TE 1.1 ms, TR 2.5 ms, flip angle 25°, FOV 400×400 mm^2, readout bandwidth 980 Hz/pixel, matrix 358×512, voxel size 1.4×1.0×3 mm^3, 72 partitions, GRAPPA factor of 3, and a 20-25 s acquisition time.

MR data acquisition was started at the time of contrast material arrival in the ascending aorta and patients were asked to hold their breath following inspiration.

After data acquisition, image processing was performed on a separate 3D workstation (Leonardo, Siemens Medical Solutions) with standard commercial software using a maximum intensity projection (MIP) algorithm. The entire 3D volume was reconstructed by overlapping thin MIP sub-volumes (10-mm thick, overlapped by 9 mm) in coronal, sagittal, and axial planes.

MRA image analysis

Two radiologists with at least 5 years' experience in cardiovascular imaging evaluated the MRA datasets independently. Separate reading sessions were organized for both readers by the study coordinator, who attended all reading sessions. For each patient, there was a 1-week window period between the readings of CE-MRA and SSFP MRA datasets to avoid recall bias. Using source-partition images for both datasets, all SSFP MRA datasets were read at the first session, followed by all CE-MRA datasets at the second session.

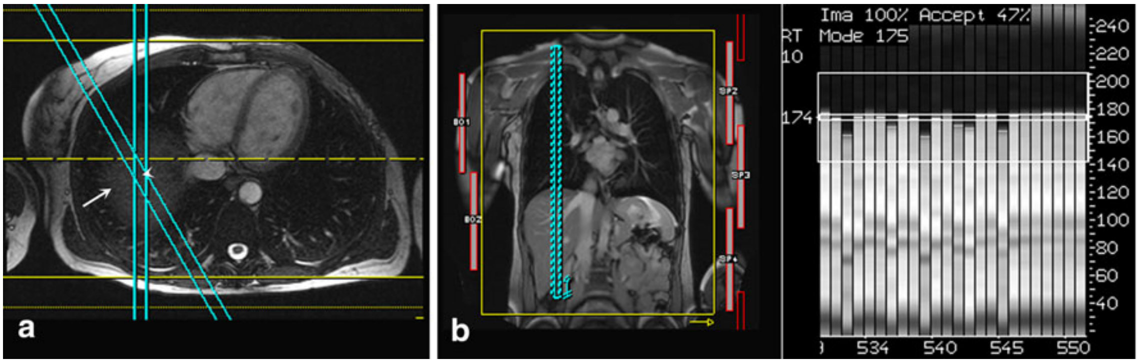

Fig. 1 Depiction of the navigator gating, FOV, and data acquisition of 3D SSFP MRA of thoracic aorta without intravenous contrast material. A column of tissue (**a**, *arrowhead*) at the intersection of two slices over the diaphragm (**a**, *arrow*) generates a spin-echo that is utilized to track the diaphragm (lung-liver interface). Coronal scout image of the whole chest (**b**) illustrates the imaging volume, which is typically a large FOV for this technique (**b**, *yellow box*), the navigator echo (**b**, *dotted blue bars*), and the right-to-left phase-encoding direction (**b**, *yellow arrow*). The end-expiratory position of the diaphragm is tracked by the narrow 4-mm adaptive gating window, which is highlighted on the *narrow central bar* (**c**). Data falling outside this narrow window were rejected (**c**, *central narrow bar*). The absolute distance scale of the diaphragm is shown on the *y*-axis (**c**). The 3D navigator gated motion adaptive sequence utilizes the reference position of the diaphragm (174 in this case) to place the gating window to track the end-expiratory position of the diaphragm. Liver and pulmonary parenchyma are indicated by *white and gray bars*, respectively (**c**)

Qualitative analysis

Datasets of unenhanced SSFP and conventional CE-MRA of the thoracic aorta were evaluated for visibility and sharpness of aortic segments, artifacts, and any abnormal findings such as aortic aneurysm (diameter greater than 4 cm), dissection, coarctation, vasculitis, intramural hematoma, or penetrating ulcer. For analysis, the thoracic aorta was divided into nine segments: segment 1, aortic annulus; segment 2, sinus of Valsalva; segment 3, sino-tubular junction; segment 4, ascending aorta; segment 5, aortic arch; segment 6, descending aorta; and segments 7–9, origins of supra-aortic arteries including right brachiocephalic, left common carotid, and left subclavian arteries.

Visibility and sharpness of the segments were graded using a four-point scale (0, not visualized; 1, poorly defined with substantial blurring such that aortic abnormalities could not be confidently evaluated; 2, well defined with mild blurring such that aortic abnormalities could be confidently diagnosed; 3, excellent definition without blurring with high confidence in the diagnosis of aortic abnormalities). Visibility of a segment was rated to be diagnostic (score ≥ 2) if the readers were confident that clinically relevant diagnostic information could be gained from the visualized segment. Presence of artifact was rated on a four-point scale (0, no artifact; 1, mild artifact not interfering with diagnostic content; 2, moderate artifact degrading diagnostic content; 3, severe artifact resulting in non-diagnostic images).

Quantitative analysis

For diseased segments, the largest diameter of the aneurysmal aortic segment and the smallest diameter of the coarctation were measured by one reader and compared on both MRA datasets. Measurements on SSFP MRA were compared with CE-MRA datasets.

SNR and contrast-to-noise ratio (CNR) were measured and compared in the aortic root, ascending aorta, aortic arch, and descending aorta on both datasets by one reader. SNR was calculated as the signal intensity from the desired region of interest (ROI) divided by the standard deviation of the background noise, which was determined by a mean value from six extra-corporeal regions. For evaluation of CNR, the reference ROI was placed over the adjacent muscle in the neck. CNR was measured as the difference between the signal intensity in the venous segment and the muscle tissue divided by the standard deviation of the background noise.

Statistical analysis

Sensitivity, specificity, positive and negative predictive values, and diagnostic accuracy of SSFP MRA for the detection of aortic abnormalities were evaluated. Pearson correlation coefficient, Bland-Altman plot, and paired *t*-test were used to analyze the quantitative measurements of the diseased segments.

Mann-Whitney *U*test was used to test for a statistical difference between segmental visibility and sharpness ratings between unenhanced SSFP and conventional CE-MRA. The inter-observer difference was analyzed with the Wilcoxon signed rank test. Inter-observer agreement for visibility between the two readers was determined by calculating Cohen's kappa (κ) using a weighted kappa test (poor agreement, $\kappa=0$; slight agreement, $\kappa=0.01-0.2$; fair agreement, $\kappa=0.21-0.4$; moderate agreement, $\kappa=0.41-0.6$; good agreement, $\kappa=0.61-0.8$; and excellent agreement, $\kappa=0.81-1$). A paired *t*-test was used to evaluate any difference between the SNR and CNR of the two datasets. Statistical analysis was performed using SPSS (version 14, Chicago, Ill., USA) and MedCalc (version 11, Mariakerke, Belgium) software.

Results

No patient was excluded from the study based on exclusion criteria. Both unenhanced SSFP and CE-MRA examina-

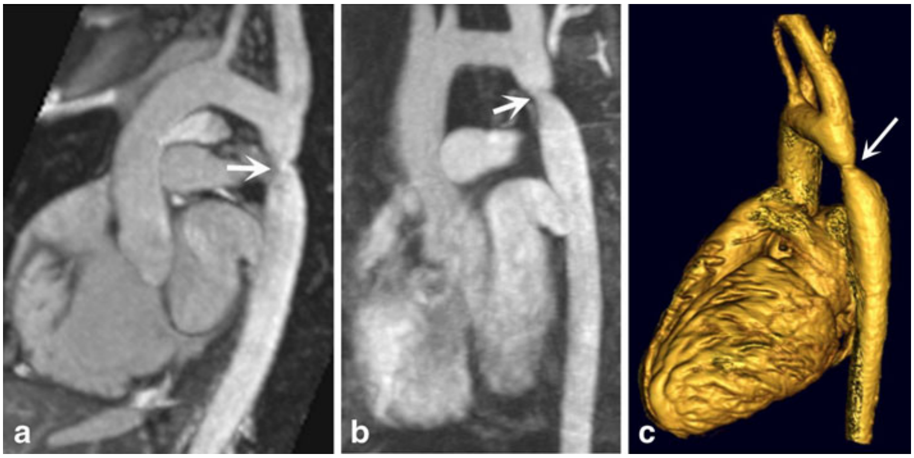

Fig. 2 A 34-year-old male patient with aortic coarctation. Oblique sagittal view of unenhanced 3D SSFP MRA (**a**) and CE-MRA (**b**) demonstrate the significant focal stenosis of the distal transverse arch consistent with aortic coarctation (**a** and **b**, *arrow*). Three-dimensional volume rendered image also shows the coarctation (**c**, *arrow*)

tions were performed successfully in all patients. None of the unenhanced navigator-gated SSFP acquisitions were repeated.

Findings

The abnormal findings (Figs. 2, 3, 4 and 5) included aortic root aneurysm ($n=19$), ascending aortic aneurysm ($n=17$), aortic arch aneurysm ($n=6$), descending aortic aneurysm ($n=5$), coarctation ($n=14$), dissection without involvement of the major aortic branches ($n=12$), intramural hematoma ($n=11$), mural thrombus in the aortic arch ($n=1$), aortic graft ($n=6$; four for aneurysm repair and two for type I dissection repair), and penetrating aortic ulcer ($n=9$) (Table 1). All findings on SSFP MRA were confirmed on CE-MRA datasets in all patients. There were no false positives or negatives on SSFP MRA, yielding 100% sensitivity, specificity, positive and negative predictive values, and diagnostic accuracy for the detection of aortic disease.

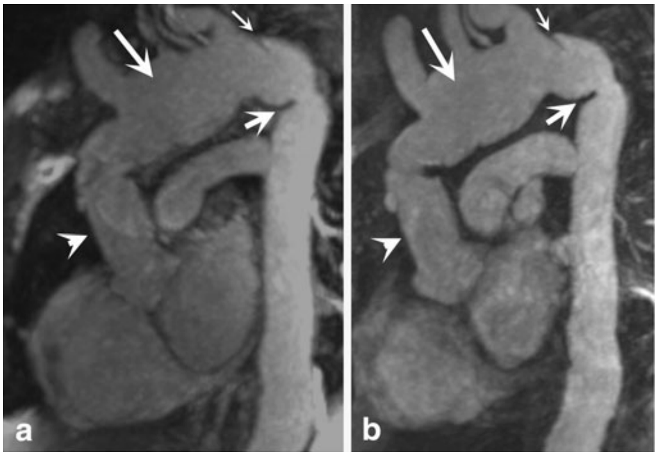

Fig. 4 A 44-year-old female patient with a history of type I aortic dissection and status post-ascending aortic graft. Oblique sagittal views of non-contrast SSFP MRA (**a**) and conventional CE-MRA (**b**) demonstrate the ascending aortic graft (**a** and **b**, *arrowhead*), aneurysmal native aortic arch (**a** and **b**, *large arrow*), a small residual dissection flap in the distal aortic arch (**a** and **b**, *thin arrow*), and kinking at the junction of the aortic arch and descending aorta (**a** and **b**, *small arrow*)

Qualitative image analysis

Unenhanced SSFP MRA

A total of 450 (100%) aortic segments were visualized by both readers on unenhanced-enhanced SSFP MRA datasets. Both readers identified 450 (100%) segments with grades for definition within the diagnostic range (grades 2 and 3), and no segments with insufficient definition to make a diagnosis (grades 0 and 1). There was no statistically significant difference in segmental visibility and sharpness grades assigned by the two readers ($P > 0.05$). The overall inter-observer agreement for the assigned visibility grades was excellent ($\kappa=0.89$; 95% confidence interval: 0.85–0.93) (Table 2).

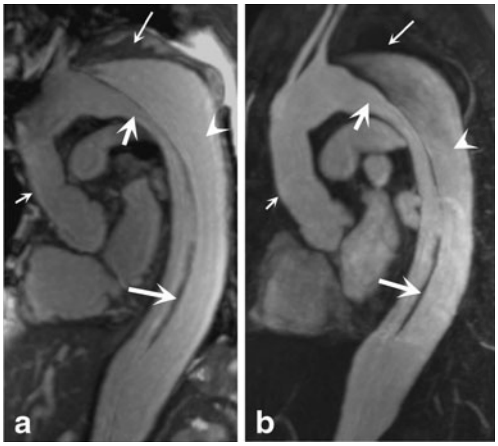

Fig. 3 A 51-year-old male patient, status post-surgical repair of type I dissection with residual intimal flap in the arch and descending aorta. Sagittal oblique image from non-contrast 3D SSFP MRA (**a**) and corresponding sagittal oblique image from CE-MRA (**b**) demonstrate the ascending aortic surgical graft (**a** and **b**, small thin arrow), anterior true lumen (**a** and **b**, *small arrow*), posterior false lumen (**a** and **b**, *arrowhead*), aneurysmal dilatation of the distal transverse arch, and the residual low signal intimal flap (**a** and **b**, *large arrow*). Mural thrombus in the false lumen of the aortic arch (**a** and **b**, *large thin arrow*) is better appreciated on non-contrast SSFP MRA

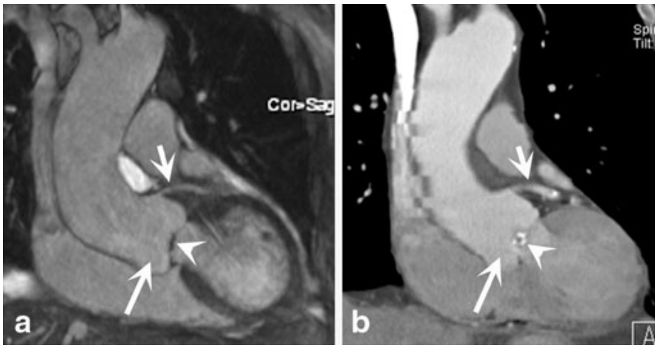

Fig. 5 A 64-year-old male patient with aortic root aneurysm. Coronal image from unenhanced SSFP MRA (**a**) demonstrates aneurysm of the aortic root (**a**, *large arrow*) and thickening of the aortic valve (**a**, *arrowhead*) without evidence of motion artifact. Excellent correlation with cardiac gated coronal CT angiography (**b**) for the aortic root aneurysm (**b**, *large arrow*) and aortic valve thickening (**b**, *arrowhead*). Left main coronary artery is also clearly visualized with both techniques because of cardiac gating (**a** and **b**, *small arrow*). Step artifacts are noted in CTA but not in SSFP MRA

Table 1 Abnormal findings in the thoracic aorta on SSFP MRA and CE-MRA

Findings	Number of patients
Aortic root aneurysm	19
Ascending aorta aneurysm	17
Aortic arch aneurysm	6
Descending aorta aneurysm	5
Aortic coarctation	14
Intramural hematoma	11
Aortic dissection	12
Aortic graft	
Penetrating aortic ulcer	9
Mural thrombus in aortic arch	1

Sensitivity, specificity, positive and negative predictive values, and diagnostic accuracy of SSFP MRA were 100%, considering CE-MRA as the reference standard

Conventional CE-MRA

A total of 450 (100%) aortic segments were visualized by both readers on CE-MRA datasets. Reader 1 identified 393 (87.3%) segments with grades for definition within the diagnostic range (grades 2 and 3), and 57 (12.7%) segments with insufficient definition to make a diagnosis (grades 0 and 1). Reader 2 identified 396 (88%) segments with grades for definition within the diagnostic range (grades 2 and 3), and 54 (12%) segments with insufficient definition to make a diagnosis (grades 0 and 1). There was no statistically significant difference in segmental visibility and sharpness grades assigned by the two readers ($P>0.05$). The overall inter-observer agreement for the assigned visibility grades was excellent ($\kappa=0.85$; 95% confidence interval: 0.76–0.94) (Table 2).

Comparison of assigned visibility and sharpness scores between SSFP MRA and CE-MRA for both readers using the Mann-Whitney *U*-test revealed significantly higher visibility scores for the aortic root (annulus, sinus of Valsalva, and sino-tubular junction) on SSFP MRA compared with CE-MRA ($P<0.001$ for both readers). No statistically significant difference existed between the datasets for the visibility and sharpness scores of any other segment for each reader ($P>0.05$ for both readers).

On SSFP MRA datasets, reader 1 (reader 2) identified mild motion artifact in the aortic root (annulus, sinus of Valsalva, and sino-tubular junction), $n=2$ (2); ascending aorta, $n=1$ (2); aortic arch, $n=1$ (0); descending aorta, $n=1$ (1); origins of supra-aortic arteries, $n=3$ (1). Neither reader identified moderate or severe artifact on any of the SSFP datasets. Similarly, on CE-MRA datasets, reader 1 (2) identified motion artifact in the aortic root [moderate, $n=42$ (39); mild, $n=61$ (63)], ascending aorta [mild, $n=8$ (7)], aortic arch [mild, $n=1$ (1)], descending aorta [mild, $n=2$ (1)], and the origins of supra-aortic arteries [mild, $n=4$ (3)]. Neither reader identified severe artifact on any of the CE-MRA datasets.

Quantitative image analysis

Details of SNR and CNR values for aortic segments are given in Table 3. Statistical analysis with paired *t*-test revealed significantly higher SNR ($P<0.01$) and CNR ($P<0.01$) values for all aortic segments on SSFP MRA compared with CE-MRA. Comparison of measurements

Table 2 Thoracic aorta visibility and sharpness scores on unenhanced SSFP MRA and high-resolution CE-MRA for both readers

Segment	SSFP MRA reader 1(2)				CE-MRA reader 1(2)			
	Grade 1	Grade 2	Grade 3	Median	Grade 1	Grade 2	Grade 3	Median
Aortic annulus[a]	0(0)	5(6)	45(44)	3(3)	20(21)	29(27)	1(2)	2(2)
Sinus of Valsalva[a]	0(0)	4(3)	46(47)	3(3)	19(17)	28(30)	3(3)	2(2)
Sino-tubular junction[a]	0(0)	3(3)	47(47)	3(3)	18(16)	28(30)	4(4)	2(2)
Ascending aorta	0(0)	2(2)	48(48)	3(3)	0(0)	6(7)	44(43)	3(3)
Aortic arch	0(0)	1(0)	49(50)	3(3)	0(0)	1(2)	49(48)	3(3)
Descending aorta	0(0)	0(0)	50(50)	3(3)	0(0)	1(0)	49(50)	3(3)
Origin of left common carotid	0(0)	0(0)	50(50)	3(3)	0(0)	1(1)	49(49)	3(3)
Origin of brachiocephalic	0(0)	1(0)	49(50)	3(3)	0(0)	0(1)	50(49)	3(3)
Origin of left subclavian	0(0)	1(1)	49(49)	3(3)	0(0)	0(0)	50(50)	3(3)

Data are number of segments. The four-point scale for evaluation of visualization and sharpness of aortic segments was as follows: 0, not visualized; 1, poorly defined with substantial blurring such that aortic abnormalities could not be confidently evaluated; 2, well defined with mild blurring such that aortic abnormalities could be confidently diagnosed; 3, excellent definition without blurring with high confidence for the diagnosis of aortic abnormalities. The overall inter-observer agreement for the visibility scores assigned by the readers was excellent for SSFP MRA ($\kappa=0.89$) and CE-MRA ($\kappa=0.85$) datasets

[a] The visibility and sharpness of aortic root segments including the annulus, sinus of Valsalva, and sino-tubular junction were significantly higher on SSFP MRA than on CE-MRA ($P<0.05$ for all)

Table 3 SNR and CNR in thoracic aortic segments on unenhanced SSFP and high-resolution CE-MRA. All values are presented as mean ± standard deviation

	Unenhanced SSFP MRA [a]		High-resolution CE-MRA[a]	
	SNR	CNR	SNR	CNR
Aortic root	115.7±34.2	95.8±29.7	85.9±28.7	66.3±23.3
Ascending aorta	121.3±37.6	103.2±30.6	96.1±29.1	79.1±25.2
Aortic arch	124.1±36.2	105.5±32.7	98.8±28.1	77.9±22.6
Descending aorta	122.2±33.8	104.9±30.9	99.2±25.5	78.3±24.4

SNR and CNR values are significantly higher in all aortic segments on SSFP MRA compared with conventional high-resolution CE-MRA (*P*<0.01 and *P*<0.01, respectively)

for the diameters of diseased segments between SSFP and CE-MRA showed a significant correlation (*r*=0.99) with no statistically significant difference (*P*<0.001) (Fig. 6a). A Bland-Altman plot revealed a mean difference of 0.16 mm (limits of agreement, -0.73 to 1.05 mm), and no more than 1.0 mm absolute difference between the measurements (Fig. 6b). Based on quantitative measurements five patients underwent surgical intervention (coarctation repair, *n*=2; aneurysm repair, *n*=3) and all other patients were managed conservatively.

Discussion

Our study results indicate that free-breathing ECG-gated 3D SSFP MRA of the thoracic aorta affords high sensitivity, specificity, and diagnostic accuracy in the diagnosis of common and important aortic diseases without administration of IV gadolinium. This technique provides high spatial resolution unenhanced MRA of the thoracic aorta with excellent image quality of all aortic segments including the aortic root. This is clinically important to assess the origin of the coronary arteries in relation to the aortic root. Normal anatomy of the thoracic aorta and aortic diseases, including aortic root aneurysm, aortic aneurysm, aortic coarctation, and aortic dissection, were confidently evaluated on SSFP MRA with excellent correlation with CE-MRA.

In patients with an aortic aneurysm (*n*=47), unenhanced SSFP MRA accurately showed the site, extent, and size of the aneurysm. These findings were confirmed on CE-MRA. Aortic dissection was accurately diagnosed on SSFP MRA in 12 patients. False and true lumens were clearly demonstrated. There was no evidence for involvement of major aortic branches on SSFP MRA which was subsequently confirmed on CE-MRA. There were ten patients with type II dissection, one patient with ascending aortic graft repair for type I dissection complicated by aortic arch aneurysm and a small residual dissection flap in the distal aortic arch (Fig. 4), and one patient with an ascending aortic graft repair for type I dissection with residual dissection flap in the distal aortic arch and

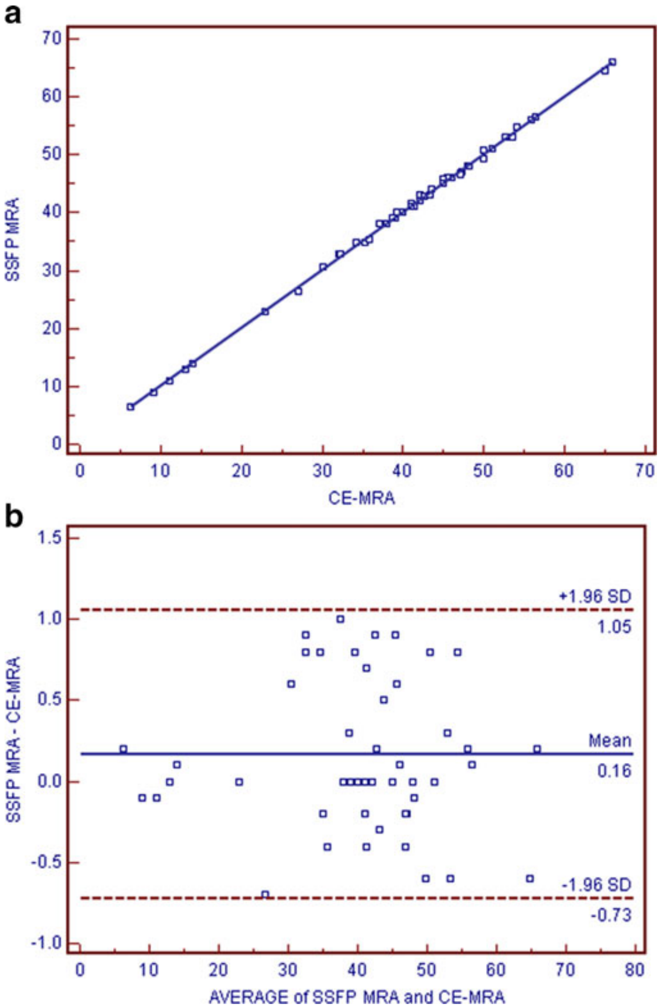

Fig. 6 **a** Graph showing significant correlation between unenhanced SSFP MRA and conventional CE-MRA for quantitative measures of the largest diameter of the aortic aneurysm and the smallest diameter of the coarctation (*r*=0.99, *P*<0.001). **b** Bland–Altman plot for evaluation of the differences between measurements of the aortic diameter in diseased segments on unenhanced SSFP MRA and CE-MRA. All differences fall within two standard deviations of the mean difference (0.16 mm) with no more than 1 mm absolute difference between measurements

descending aorta. In the same patient, a large mural thrombus in the false lumen was clearly depicted on SSFP MRA (Fig. 3). CE-MRA provides information regarding the aortic lumen and not the aortic wall, whereas SSFP MRA depicts both the aortic lumen and wall. Although not evaluated in this study, the SSFP sequence has an advantage over CE-MRA in the assessment of aortic wall thickness, mural thrombus, and mural hematoma.

Coarctation of the aorta was confidently evaluated in 14 patients on both SSFP and CE-MRA datasets. One patient underwent surgical stent placement. Unenhanced SSFP MRA clearly depicted an ascending aortic surgical graft in six patients (aneurysm repair, n=4; dissection repair, n=2) without evidence of graft complications such as pseudoaneurysm, aneurysm, stenosis, or infection.

Technical evaluation of image quality showed no statistically significant difference in segmental visibility and sharpness of the ascending aorta, aortic arch, and descending aorta between SSFP and CE-MRA datasets. However, for the aortic root, segmental visibility was higher for SSFP than for CE-MRA. Sufficient SNR and CNR values were achieved on SSFP MRA to support confident evaluation of all segments.

Contrast-enhanced high spatial resolution 3D MRA has been shown to provide excellent image quality for the accurate diagnosis and follow-up of aortic disease [1–4]. This technique requires administration of IV gadolinium-based contrast agent and patient cooperation for breath-holding. In certain clinical conditions such as obesity, poor peripheral IV access, systemic hypovolemia due to acute blood loss or volume sequestration, and pregnancy, injection of IV contrast material may be contraindicated or technically not feasible in a timely manner. In addition, the risk of NSF in patients with advanced renal disease in the setting of high-dose gadolinium-based contrast agent exposure [7–9] is raising concerns among physicians regarding the widespread use of these agents. Furthermore, patient cooperation for breath-holding may be sub-optimal in patients with cardiopulmonary disease.

Several unenhanced MRI strategies have been implemented for imaging the thoracic aorta including SSFP, spin-echo, gradient echo, time-of-flight, and phase-contrast imaging [10, 12, 13, 18, 19]. Spin-echo, time-of-flight, and phase-contrast sequences have limitations including longer acquisition times and poor image quality. Spin-echo and time-of-flight sequences are particularly susceptible in areas of slow, turbulent, or in-plane flow such as in aneurysms [10, 18, 19].

The high T2/T1 signal ratio inherent to SSFP sequences enhances the contrast between blood and the adjacent tissue. In addition, with a high and uniform vascular SNR, short acquisition time, and reduced repetition time, SSFP has the potential for excellent evaluation of blood vessels [11, 20]. Pereles et al. [21] successfully implemented a single-shot 2D SSFP technique with selective RF excitation for the evaluation of thoracic aortic aneurysms and dissections in less than 4 min. Nevertheless, this 2D SSFP sequence and the several unenhanced MRI sequences referred to above are limited in providing 3D information of the thoracic aorta.

In our study, we utilized a 3D SSFP sequence with a non-selective RF pulse over a large FOV (400×400 mm^2), which enabled us to implement a very short TR/TE of 2.3 ms/1.0 ms [12, 13]. The use of a non-selective RF excitation approach allowed us to minimize the susceptibility of the SSFP sequence to B0 magnetic field inhomogeneities and out of slice contributions—the major contributors to image artifacts. In this non-selective approach, compared with the selective excitation techniques implemented in previous studies [22, 23], the imaging slab needs to cover the entire chest. This implies thicker imaging slabs and results in longer acquisition times. However, the resultant benefit of a shorter TR and minimal slice oversampling due to diminished slice profile issues partially compensated for the prolonged imaging time. In addition, we implemented motion adaptive gating for respiratory drifts with resultant acquisition of data only during the end-expiratory phase. Furthermore, to improve the spatial resolution, we combined our SSFP sequence with parallel imaging using a GRAPPA factor of 2 [17]. Thus, the average image acquisition time for this sequence was 7±2 min (range; 5–10 min) which is considerably longer than CE-MRA which takes approximately 20–25 s. However, in CE-MRA, we need additional time to establish venous access, set up contrast material for injection, and post-process the images. It is conceivable that the prolonged acquisition time of the 3D SSFP MRA was also due to cardiac gating.

François et al. [24] have studied the image quality of a similar 3D SSFP MRA technique for assessment of thoracic aorta in comparison with CE-MRA, and shown no difference between the two techniques in terms of image quality. However, because of the limited number of patients and thoracic aortic abnormalities, the authors were not able to evaluate the diagnostic performance of the SSFP MRA.

Measured SNR and CNR values were noted to be significantly higher on SSFP MRA than on CE-MRA. Furthermore, the use of cardiac-triggering resulted in less motion artifact and higher image quality of the aortic root compared with CE-MRA. Excellent, or diagnostic, image quality was achieved for 100% of aortic segments on SSFP MRA, which allowed us to confidently evaluate all aortic disease with a diagnostic accuracy of 100% using CE-MRA as the reference standard. Analysis of quantitative orthogonal measurements for the diseased segments revealed almost perfect correlation between the two MRA datasets (Fig. 6a) with no statistically significant difference. This suggests that unenhanced SSFP MRA has the potential to provide accurate and reliable assessment of the severity of aortic coarctation, dilatation, and aneurysms, which is essential in clinical decision making.

Our study has limitations. No correlation was made with the “gold standard” provided by DSA because at our institution this procedure is not utilized as a primary diagnostic or follow-up technique, but only as an interventional procedure. We did not evaluate the use of this sequence in patients with acute aortic syndromes or in the inpatient setting. These patients are generally evaluated with CTA and may not be suitable for monitoring in the MR environment. Furthermore, CE-MRA examinations were not cardiac-gated. This has resulted in lower image quality for the aortic root segments compared with SSFP MRA. Finally, larger voxel size on SSFP MRA and a higher acceleration factor of 3 implemented on CE-MRA, altered the SNR and CNR values in favor of unenhanced SSFP MRA, and a true comparison of SNR and CNR values could not be performed between these datasets, as calculation of the corrected estimate of SNR and CNR is complicated [25–28]. However, when the determination of proximal coronary artery disease is not critical and when assessment of vascular visibility is needed, estimates of SNR and CNR are not prohibited entirely [25].

In conclusion, free-breathing, navigator-gated, ECG-triggered, 3D SSFP MRA with non-selective RF excitation is a promising technique and affords high sensitivity, specificity, and diagnostic accuracy in the assessment of aortic diseases without the need for intravenous contrast material. This technique may be an alternative non-invasive approach to assess or screen for thoracic aortic disease in certain patients at high risk of developing gadolinium-based contrast material-related complications, difficulty in breath-holding, difficult venous access, and during pregnancy without exposure to ionizing radiation or intravenous contrast material. Further studies, preferably multicentric, with optimization of sequence parameters, are warranted to evaluate the diagnostic accuracy of SSFP MRA of the thoracic aorta and clinical outcome in a larger patient cohort.

Acknowledgements The authors thank Apar Singhal MD, a research volunteer, and Francine Cobla, Glen Nyborg, and Sergio Godinez, cardiovascular MRI technologists, for their contribution to this project at UCLA.

References

1. Gebker R, Gomaa O, Schnackenburg B, Rebakowski J, Fleck E, Nagel E (2007) Comparison of different MRI techniques for the assessment of thoracic aortic pathology: 3D contrast enhanced MR angiography, turbo spin-echo and balanced steady state free precession. Int J Cardiovasc Imaging 23(6):747–756
2. Groves EM, Bireley W, Dill K, Carroll TJ, Carr JC (2007) Quantitative analysis of ECG-gated high-resolution contrast-enhanced MR angiography of the thoracic aorta. AJR Am J Roentgenol 188(2):522–528
3. Prince MR, Narasimham DL, Jacoby WT et al (1996) Three-dimensional gadolinium-enhanced MR angiography of the thoracic aorta. AJR Am J Roentgenol 166:1387–1397
4. Krinsky GA, Reuss PM, Lee VS et al (1999) Thoracic aorta: comparison of single-dose breath-hold and double-dose non-breath-hold gadolinium-enhanced three-dimensional MR angiography. AJR Am J Roentgenol 173:145–150
5. Lawler LP, Fishman EK (2003) Multi-detector row computed tomography of the aorta and peripheral arteries. Cardiol Clin 21:607–629
6. Chiles C, Carr JJ (2005) Vascular diseases of the thorax: evaluation with multidetector CT. Radiol Clin North Am 43:543–569
7. Kanal E, Broome DR, Martin DR, Thomsen HS (2008) Response to the FDA’s May 23, 2007, nephrogenic systemic fibrosis update. Radiology 246(1):11–14
8. Marckmann P, Skov L, Rossen K, Heaf JG, Thomsen HS (2007) Case-control study of gadodiamide-related nephrogenic systemic fibrosis. Nephrol Dial Transplant 22(11):3174–3178
9. Sadowski EA, Bennett LK, Chan MR et al (2007) Nephrogenic systemic fibrosis: risk factors and incidence estimation. Radiology 243(1):148–157
10. Russo V, Renzulli M, Buttazzi K, Fattori R (2006) Acquired diseases of the thoracic aorta: role of MRI and MRA. Eur Radiol 16(4):852–865
11. Fuchs F, Laub G, Othomo K (2003) TrueFISP—technical considerations and cardiovascular applications. Eur J Radiol 46:28–32
12. Tomasian A, Lohan DG, Laub G, Singhal A, Finn JP, Krishnam MS (2008) Noncontrast 3D steady state free precession magnetic resonance angiography of the thoracic central veins using nonselective radiofrequency excitation over a large field of view: initial experience. Invest Radiol 43(5):306–313
13. Krishnam MS, Tomasian A, Deshpande VS et al (2008) Non-contrast 3D SSFP MR angiography of the whole chest using non-selective RF excitation over a large field of view: comparison with single-phase 3D contrast-enhanced MRA. Invest Radiol 43(6):411–420
14. Brittain JH, Hu BS, Wright GA, Meyer CH, Macovski A, Nishimura DG (1995) Coronary angiography with magnetization-prepared T2 contrast. Magn Reson Med 33(5):689–696
15. Shea SM, Deshpande VS, Chung YC (2002) Three-dimensional true-FISP imaging of the coronary arteries: improved contrast with T2-preparation. J Magn Reson Imaging 15:597–602

16. Deshpande VS, Krishnam MS, Ruehm SG et al (2006) Non-contrast MR angiography of the heart and great vessels using SSFP with non-selective excitation (abstract). In: Proceedings of the Fourteenth Scientific Meeting of the International Society for Magnetic Resonance in Medicine. International Society for Magnetic Resonance in Medicine, Seattle, p 383
17. Griswold MA, Jakob PM, Heidemann RM et al (2002) Generalized autocalibrating partially parallel acquisitions (GRAPPA). Magn Reson Med 47:1202–1210
18. Reddy GP, Higgins CB (2000) MR imaging of the thoracic aorta. Magn Reson Imaging Clin N Am 8(1):1–15
19. Summers RM, Sostman HD, Spritzer CE et al (1996) Fast spoiled gradient-recalled MR imaging of thoracic aortic dissection: preliminary clinical experience at 1.5 T. Magn Reson Imaging 14:1–9
20. McCarthy RM, Deshpande VS, Beohar N et al (2007) Three-dimensional breathhold magnetization-prepared TrueFISP: a pilot study for magnetic resonance imaging of the coronary artery disease. Invest Radiol 42:665–670
21. Pereles FS, McCarthy RM, Baskaran V, Carr JC et al (2002) Thoracic aortic dissection and aneurysm: evaluation with non-enhanced TrueFISP MR angiography in less than 4 minutes. Radiology 223:270–274
22. Sorensen TS, Körperich H, Greil GF et al (2004) Operator-independent isotropic three-dimensional magnetic resonance imaging for morphology in congenital heart disease: a validation study. Circulation 110:163–169
23. Bi X, Deshpande V, Carr J, Li D (2006) Coronary artery magnetic resonance angiography (MRA): a comparison between the whole-heart and volume targeted methods using a T2-prepared SSFP sequence. J Cardiovasc Magn Reson 8:703–707
24. François CJ, Tuite D, Deshpande V, Jerecic R, Weale P, Carr JC (2008) Unenhanced MA angiography of the thoracic aorta: initial clinical evaluation. AJR Am J Roentgenol 190 (4):902–906
25. Muthupillai R, Smink J, Hong S, Ravindran R, Lee VV, Flamm SD (2006) SENSE or k-MAG to accelerate free breathing navigator-guided coronary MR angiography. AJR Am J Roentgenol 186:1669–1675
26. Pruessmann KP, Weiger M, Scheidegger MB, Boesinger P (1999) SENSE: sensitivity encoding for fast MRI. Magn Reson Med 42:952–962
27. Kellman P, McVeigh ER (2005) Image reconstruction in SNR units: a general method for SNR measurement. Magn Reson Med 54:1439–1447
28. Glockner JF, Hu HH, Stanley DW, Angelos L, King K (2005) Parallel MR imaging: a user's guide. Radiographics 25:1279–1297